

X-ray Spectra and Multiwavelength Machine Learning Classification for Likely Counterparts to *Fermi* 3FGL Unassociated Sources

STEPHEN KERBY,¹ AMANPREET KAUR,¹ ABRAHAM D. FALCONE,¹ MICHAEL C. STROH,² ELIZABETH C. FERRARA,^{3,4}
JAMIE A. KENNEA,¹ AND JOSEPH COLOSIMO¹

¹*Department of Astronomy and Astrophysics*

Pennsylvania State University University Park, PA 16802, USA

²*Center for Interdisciplinary Exploration and Research in Astrophysics (CIERA), Northwestern University, Evanston, IL 60201, USA*

³*NASA Goddard Space Flight Center, Greenbelt, MD 20771, USA*

⁴*Department of Astronomy, University of Maryland College Park, MD 20742, USA*

(Received Sep 09 2020; Revised Dec 10 2020; Accepted Jan 9, 2021)

Submitted to AJ

ABSTRACT

We conduct X-ray spectral fits on 184 likely counterparts to *Fermi*-LAT 3FGL unassociated sources. Characterization and classification of these sources allows for more complete population studies of the high-energy sky. Most of these X-ray spectra are well fit by an absorbed power law model, as expected for a population dominated by blazars and pulsars. A small subset of 7 X-ray sources have spectra unlike the power law expected from a blazar or pulsar and may be linked to coincident stars or background emission. We develop a multiwavelength machine learning classifier to categorize unassociated sources into pulsars and blazars using gamma- and X-ray observations. Training a random forest procedure with known pulsars and blazars, we achieve a cross-validated classification accuracy of 98.6%. Applying the random forest routine to the unassociated sources returned 126 likely blazar candidates (defined as $P_{bzt} \geq 90\%$) and 5 likely pulsar candidates ($P_{bzt} \leq 10\%$). Our new X-ray spectral analysis does not drastically alter the random forest classifications of these sources compared to previous works, but it builds a more robust classification scheme and highlights the importance of X-ray spectral fitting. Our procedure can be further expanded with UV, visual, or radio spectral parameters or by measuring flux variability.

Keywords: catalogs — surveys

1. INTRODUCTION

The bulk of the 3033 sources in the *Fermi* Gamma-ray Space Telescope - Large Area Telescope (*Fermi*-LAT) 3FGL catalog fall into one of two classes: extragalactic blazars or nearby pulsars (Acero et al. 2015). A small number of other identified sources include supernova remnants, X-ray binaries, and starburst galaxies (Ferrara et al. 2015). However, 1010 3FGL sources are “unassociated”, without a confident astrophysical identification with a known pinpointed source, or with several competing astronomical explanations within the gamma-ray detection area. Based on the dominance of blazars and pulsars among identified 3FGL sources, many of these unassociated sources are likely blazars and pulsars. Capturing these unassociated and heretofore unclassified sources would create a more complete

all-sky sample of various classes of objects, particularly blazars.

Categorizing the blazars and pulsars in the 3FGL unassociated list is an important step towards confident population studies of both classes. The *Fermi*-LAT unassociated sources might include blazars that are lower luminosity or higher redshift than their more easily detected and identified cousins in the established 3FGL blazar catalog (Ferrara et al. 2015). Therefore, pursuing the classification of the 3FGL unassociated sources will help build a more complete population study, which will aid in verification and analysis of the blazar sequence (e.g., Fossati et al. 1998; Ghisellini et al. 2017) as a theoretical unifying scheme for blazars.

In a similar way, identification and classification of 3FGL unassociated sources can also lead to new pulsar candidates, a population which has included new accret-

ing pulsars in the 3FGL catalog (e.g. Wu et al. 2018; Li et al. 2018). Furthermore, in-depth analysis might show that an object suits neither blazar nor pulsar classification. Such sources might represent new gamma-ray binaries, or possibly more exotic objects (Saz Parkinson et al. 2016). The 3FGL unassociated list could contain several such objects, but classification of the blazars and pulsars that probably make up most of the unassociated sample is the first step in identifying any unique sources.

While gamma-ray observations from *Fermi*-LAT are the foundation for the 3FGL catalog, matching gamma-ray sources with X-ray counterparts and extending analysis to lower energy photons is a vital step in deeper analysis of the 3FGL sources. Recent work (Kaur et al. 2019) developed a machine learning (ML) approach to sort 217 high-S/N unassociated 3FGL sources into blazars and pulsars. The 217 unassociated sources were analyzed by combining the gamma-ray flux and photon index of each object with a coarse estimate for the X-ray flux using probable counterpart X-ray excesses from the Neil Gehrels *Swift* Observatory (aka *Swift*) (Gehrels et al. 2004). For simplicity, the X-ray fluxes used in that work assumed an X-ray photon index of $\Gamma_X = 2$ rather than conducting full spectral fits. Training an ML routine with known pulsar and blazar samples, the authors identified 173 likely blazars with $P_{b_{zr}} > 90\%$ (134 with $P_{b_{zr}} > 99\%$) and 13 likely pulsars with $P_{b_{zr}} < 10\%$ (7 with $P_{b_{zr}} < 1\%$). 31 sources from the 3FGL unassociated list defied categorization and were labeled ‘ambiguous’.

The unassociated sources examined in (Kaur et al. 2019) each had only one high-S/N X-ray excess in their gamma-ray confidence ellipse, and the majority of gamma-ray sources are expected to have counterpart X-ray sources. This is especially true of blazars, which make up the majority of the catalog. In Kaur et al. (2019) and this work we only examine gamma-ray sources with a single high-S/N ($S/N > 4$) X-ray excess in the confidence region, and for the purposes of classification, we make the initial assumption that this source is the counterpart. There may be some rare cases in which this X-ray source and the unassociated gamma-ray source do not correspond to one another, but since there is no other strong X-ray source in the Fermi error ellipse, this X-ray source is the most likely counterpart.

In this work, we expand upon ML investigations by conducting detailed X-ray spectral analysis of 184 possible X-ray counterparts of the unassociated 3FGL sources. We obtain fully fitted X-ray fluxes and photon flux power law indices using an absorbed power-law model. Our training and validation sample was drawn from known lists of *Fermi*-LAT blazars and pul-

sars which had data for all six gamma- and X-ray parameters used in our ML process (Ackermann et al. 2015; Abdo et al. 2013). Kaur et al. (2019) used a list of 217 unassociated sources for the test sample. 56 of those 217 objects later were associated with an astronomical object, so those were removed from consideration in this paper. Since then new observations have added 26 solitary X-ray excesses with high $S/N > 4$, leading to our initial list of 187 unassociated sources with one possible X-ray counterpart within the 95% confidence region of the *Fermi*-LAT unassociated source. We found three members of the 187 that were spurious contaminants from optically bright coincident stars creating optical loading in the *Swift*-XRT detector, and we excluded these three excesses from all analysis.

The goal of this work is to conduct X-ray spectral analysis for some possible counterparts to *Fermi*-LAT unassociated gamma-ray sources and to begin to build a multiwavelength classification routine. To this end we update the machine learning approach in Kaur et al. (2019) to include full X-ray spectral fits for high-S/N X-ray excesses spatially coincident with the 3FGL unassociated sources. In section 2, we discuss observations, spectral fitting, and ML processes used in our analysis, plus we describe the training, test, and research samples. Next, in section 3 we tabulate and plot parameters for the various samples and we describe our fitting and classification results. In section 4 we discuss the classifications in comparison to previous works and summarize our findings. Tables of spectral fits and ML classification results are also included.

2. OBSERVATIONS AND ANALYSIS

2.1. *Swift*-XRT Observations of 3FGL Unassociated Sources

Our sample is based on a collection that initially contained 187 *Swift* X-ray counterparts to *Fermi*-LAT 3FGL sources with high detection Signal-to-Noise (S/N) ratio ($S/N \geq 4$) and only a single X-ray excess in the 95% confidence region of the 3FGL source. As three of these counterparts (3FGL J0858.0–4843, J1050.6–6112, and J1801.5–7825) were near bright ($m_V < 8$) stars, the X-rays from those excesses are almost certainly spurious products of optical loading¹ in the *Swift*-XRT (X-ray Telescope) (Burrows et al. 2005) detector. We excluded these false detections from all further analysis. Particularly bright stars in the field of view cause optical loading in the *Swift*-XRT as optical photons contaminate the detector and introduce spuri-

¹ https://www.swift.ac.uk/analysis/xrt/optical_loading.php

ous signals. Optical loading is less likely for dimmer coincident stars.

We used the NASA HEASARC keyword interface to download all *Swift*-XRT observations within $8'$ of the centroid position of each 3FGL counterpart. Two more sources (3FGL J1216.6-0557 and 3FGL J0535.7-0617c) were matched with *Swift*-XRT observations only upon expanding the HEASARC search radius to $10'$. These sources are positioned close to the edge of the *Swift*-XRT field of view in their respective observations.

In total we collected over 500 individual *Swift*-XRT observations, capturing all 184 members of the unassociated list. All observations used the photon counting (PC) mode of the *Swift*-XRT, enabling two-dimensional imaging across the 23 arcminute XRT field-of-view. Usable *Swift*-XRT exposure times for most objects was around 4 ks, but ranged from 1 ks to over 60 ks.

We cleaned and processed each level 1 event file using `xrtpipeline` v.0.13.5 from the HEASOFT software², then merged with other observations of that particular object using `xselect` v.2.4g and `ximage` v.4.5.1 to create a single summed event list for each source plus a summed exposure map and ancillary response file using `xrtmkarf`. For each unassociated 3FGL object, we produced spectra for source and background regions using `xselect`. The source region was circular with radius 20 arcseconds, and the background region was annular with inner and outer radii of 50 and 150 arcseconds. Both regions were centered on the coordinates of the examined X-ray excess.

If the count rate in the source region of any excess exceeded 0.5 counts per second, we would draw a new annular source region with an inner radius depending on the count rate to avoid photon pile-up and saturation on the detector. The possible X-ray counterparts to 3FGL unassociated sources are faint enough that none caused pile-ups to warrant annular source regions. Adding X-ray variability to our spectral and photometric analysis of the X-ray excesses would certainly be an interesting probe into variability timescales of blazars and pulsars, but unfortunately most of the sources examined here do not have X-ray observations spanning a wide enough time range to maintain a large training, test, or research sample.

Finally, we examined the total number of counts in the source region to determine whether to use χ^2 initial spectral fitting. The Cash statistic is a useful fitting statistic for spectra with few counts, particularly in cases for which there are not sufficient counts to group

for a χ^2 fit (Cash 1976). When an excess has enough photons in its source region, we binned our data with 20 counts per bin to enable an initial χ^2 fit and also prepared a spectrum file for eventual Cash fitting. For an excess with only a few dozen detected X-ray photons, this approach would result in only one or two bins, and χ^2 fitting would produce unreliable non-Gaussian distributed fits. The Cash statistic does not require any such binning, and therefore is often used in fitting faint X-ray spectra with few counts. While the Cash statistic cannot be directly considered as a measure of goodness of fit like χ^2 , a Cash statistic similar to the degrees of freedom is a rough indicator of a reasonable fit.

2.2. Detailed X-ray Spectral Fitting

While the machine learning analysis of the X-ray counterparts to 3FGL unassociated sources in Kaur et al. (2019) assumed an X-ray photon index $\Gamma_X = 2$ to calculate X-ray flux, our archival *Swift*-XRT observations facilitated a full spectral fitting. We used `Xspec` v.12.10.1f (Arnaud 1996) to fit each spectrum. The fitting model `tbabs × cflux × powerlaw` included three nested functions: `tbabs`, `cflux`, and `powerlaw`. `cflux` calculated the total unabsorbed flux between 0.3 and 10 keV and `tbabs` modeled line-of-sight hydrogen extinction using galactic values from the `nH` lookup function described in Wilms et al. (2000).

The galactic line-of-sight extinction is fixed at the catalog value for each spectrum analyzed. `powerlaw` is a simple power law. Uncertainties on the fitted photon index and X-ray flux were jointly measured using the iterative `steppar` routine; this routine occasionally encountered numerical errors finding the error of photon indices close to zero. For these spectra we report the symmetric error generated by `fit`. Spectra with high photon counts were initially fit using χ^2 as the optimization statistic to create first guesses for Cash statistic fitting.

Comparing the new fitted fluxes to fluxes calculated assuming $\Gamma_X = 2$ provides a useful sanity check for the X-ray spectral fitting routine. Objects with fitted Γ_X close to 2 should show fitted X-ray fluxes close to the previous X-ray fluxes that assumed $\Gamma_X = 2$. Large revisions in X-ray flux should be reserved for objects with $\Gamma_X \neq 2$. Figure 1 shows this reassuring close correspondence for spectra with fitted photon indices near $\Gamma_X = 2$, while spectra with fitted indices departing from 2 show significantly corrected fluxes. All of the successful spectral fits are displayed in Table 3.

Of the eleven X-ray excesses whose fully fitted X-ray fluxes differed by more than an order of magnitude from the X-ray flux assuming $\Gamma_X = 2$, seven corresponded

² <https://heasarc.gsfc.nasa.gov/docs/software.html>

to the individually analyze unusual sources described in table 1. Of the remaining four, one with a fitted index of $\Gamma_X = 4.4$ saw a drop in X-ray flux by a factor of ten compared to $\Gamma_X = 2$ fits. This gamma-ray source (3FGL J1837.3-2403) has *Swift* exposures of such duration that at least four X-ray excesses are expected to spuriously appear in the gamma-ray confidence region, suggesting that this X-ray source is background. The remaining three X-ray excesses with radically different fitted fluxes are three of the five excesses where spectral fitting failed to converge, described above. Figure 1 excludes only the five excesses with unconverged X-ray fitting.

After fitting with a power-law model, seven excesses showed unusually high or low photon indices compared to the photon index of $\Gamma_X \sim 2$ expected for pulsars and blazars. We conducted further analysis on these excesses listed in Table 1, and they were excluded from the main ML process since they warranted individual investigation to check for coincident stars or catalog objects that might explain their spectra. Six of these seven excesses are located within a few arcseconds of dim catalogued stars in the galactic plane, possible targets for future observations to verify whether the X-ray radiation is linked to the star. A quantitative estimate of optical loading for *Swift*-XRT showed that none of the seven spectra can have count rates heavily impacted by optical loading from the nearby star, although one of the seven could have a minor contribution.

2.3. Machine Learning

While multi-wavelength spectral analysis enables comprehensive study of individual unassociated gamma-ray sources, the observations and interpretation of hundreds of such objects would pose an onerous time burden on human scientists. Fortunately, recent developments in machine learning (ML) techniques have resulted in numerous applications of ML classification schemes to *Fermi*-LAT unassociated source catalogs (Hassan et al. 2012; Saz Parkinson et al. 2016; McFadden et al. 2017). These developments are part of a wave of ML techniques promulgating into survey analysis.

In this work, we use a random forest (RF) classifier, an aggregate of many individual decision tree (DT) realizations, to classify sources into blazars and pulsars, following a procedure described in Breiman (2001). Our approach here is nearly identical to that in Kaur et al. (2019), which achieved $\approx 95\%$ accuracy with a decision tree method and $\sim 99\%$ accuracy with a random forest approach.

A detailed description of the statistics and theory of decision trees and random forests can be found in Breiman (2001). In brief, decision tree classifiers are

non-parametric supervised and trained machine learning methods. DT classifiers discriminate objects between classes by branching classes one by one at decision nodes, each node judging a single parameter of an object via an inequality. A tree is optimized using the Gini impurity index, representing the probability of a randomly selected source from the dataset being incorrectly labeled at one decision node.

The random forest approach compounds the DT method described above, generating a forest of decision trees and classifying test objects based on the average of multiple decision trees (Breiman 2001). An RF algorithm constructs numerous decision trees by randomly creating subsamples of the training dataset. The overall forest also returns the relative importance of the parameters of the training dataset.

Once the forest is fully trained, a new observation is assigned a classification probability based on the average of the classifications of each tree in the forest. Overall, the use of many decision trees in the RF routine creates a more robust analysis of test objects and prevents overfitting in a single tree from biasing results. The DT and RF methods used in this paper utilize the `sklearn` package available in Python.

2.4. Training and Test Samples

To train the RF classifier, we gathered a sample of 831 known sources, including 772 known blazars and 59 known pulsars. The sample was derived from the 3FGL catalog which provided gamma-ray properties and second Swift X-ray Point Source Catalog (2SXPS, Evans et al. 2020) which provided X-ray parameters. In addition, the X-ray properties of known pulsars were obtained from the literature search of various studies; (e.g., Marelli 2012; Saz Parkinson et al. 2016; Wu et al. 2018; Zyuzin et al. 2018). The parameters for each source included³:

- X-ray photon index Γ_X
- Gamma-ray photon index Γ_γ
- The logarithm of gamma-ray flux $\log F_\gamma$
- The logarithm of X-ray to gamma-ray flux ratio $\log F_X/F_\gamma$
- The significance of the curvature in the gamma-ray spectrum (henceforth simply *curvature*)
- The gamma-ray variability index

³ In this work, $\log x$ always refers to the logarithm in base 10 of x .

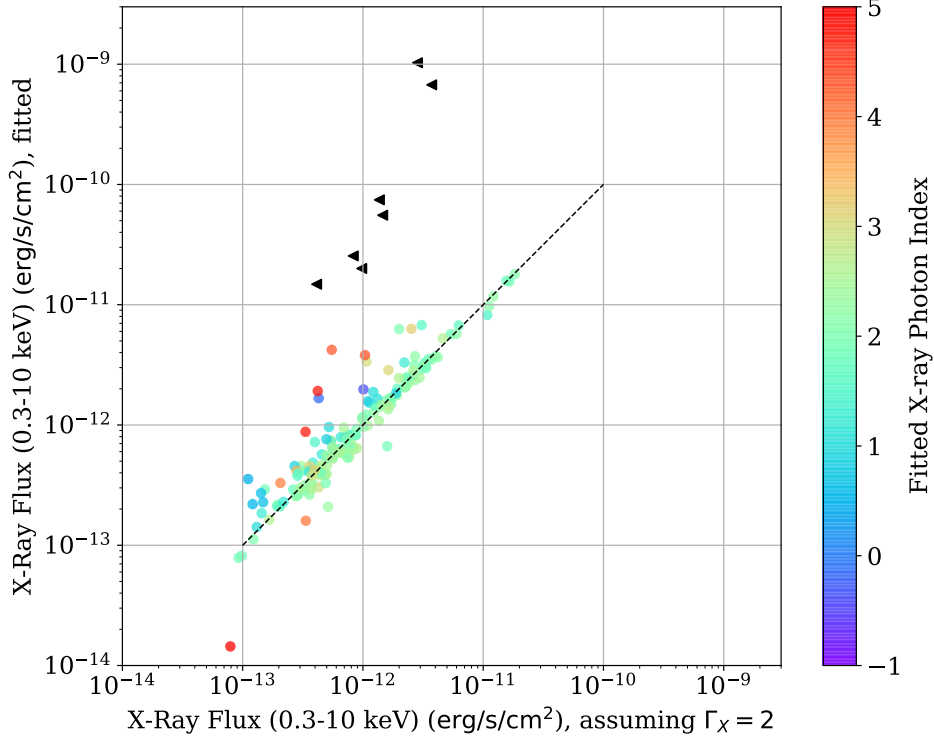


Figure 1. Fully fitted X-ray flux vs X-ray flux assuming $\Gamma_X = 2$. Points are colored based on fitted X-ray photon index. Black triangles are excesses identified as having extreme X-ray photon indices in table 1. This figure excludes the five excesses for which full X-ray fitting failed to converge.

Table 1. Seven of the possible X-ray counterparts to unassociated 3FGL sources with extreme X-ray photon indices, $\Gamma_X < -1$ or $\Gamma_X > 5$, were excluded from the main ML classification effort. We describe the spectrum of the excess and list any notable objects close to the X-ray excess via SIMBAD and NASA Extragalactic Database coordinate searches. Possible stellar counterparts include spectral type and apparent magnitude from SIMBAD if available.

3FGL Source	Γ_X	Notes
3FGL J0748.8–2208	6.29	very few counts, 2" from TYC 5993-3722-1 ($m_V = 12.4$)
3FGL J0905.6–4917	7.84	diffuse in XRT image, listed as ‘confused’ in 4FGL, 3" from 2MASS J09053033-4918382 (M4, $m_J = 9.5$)
3FGL J1329.8–6109	6.22	peaked spectrum, 10" from HD117110 (G0V, $m_V = 9.2$)
3FGL J1624.1–4700	7.42	peaked spectrum, 1" from CD-46 10711 (K1IV rotationally variable star, $m_V = 11.0$)
3FGL J1710.6–4317	6.32	peaked spectrum at 0.9 keV
3FGL J1921.6+1934	6.19	flat spectrum, 2" from HD231222 ($m_V = 10.8$)
3FGL J2035.8+4902	5.82	peaked spectrum at 0.8 keV, 5" from V* V2552 Cyg (Eclipsing binary, $m_V = 10.8$)

All the X-ray parameters were determined through our analysis as explained earlier, while the gamma ray parameters were extracted from the 3FGL catalog. The complete details of the obtained gamma-ray data and the methods are provided in [Kaur et al. \(2019\)](#).

Because there are many more known blazars than known pulsars in the training and test samples, we used Synthetic Minority Over-sampling Technique (SMOTE) ([Chawla et al. 2002](#)) to generate synthetic members of the underrepresented class (pulsars) with a k-nearest neighbors approach. Previous classification efforts have shown that seriously unbalanced training datasets can lead to trained RF classifiers that are biased against the underrepresented class ([Last et al. 2017](#)). The result of the SMOTE expansion is a catalog of known blazars and pulsars, plus artificial pulsars generated with the same distribution in parameter-space as the real pulsars, producing a catalog with a balanced number of 772 blazars and 772 pulsars. Expansion of the pulsar catalog via SMOTE is executed before the catalog is split into training and validation samples.

To optimize RF parameters such as number of individual trees and maximum tree depth, we utilized `GridSearchCV` in `sklearn v.0.20.3`. We found that 1000 decision trees splitting to a maximum depth of 15 nodes with at least one source in each leaf were required to effectively train the classifier. The reported blazar probability for each source is the fraction of the 1000 trees in which the object was classified as a blazar.

In this paper, we utilized a cross-validation method, `cross_val_predict` from `sklearn v.0.20.3` by dividing our total sample into 10 folds and then used each fold (one at a time) as a test sample. For the validation step, a RF classifier is generated using a training subsample. Members of the corresponding test subsample are then classified as a pulsar or a blazar and the generated classification is compared to the actual class label. In this way, an accuracy score for the entire RF tree is generated. This process is repeated ten times, so ten random forest classifiers are trained and each is validated in turn; the overall accuracy of the RF classifier is the average of the validation accuracy of the ten folded iterations. The overall RF accuracy obtained in this way was 98.5%.

In [Kaur et al. \(2019\)](#), the authors separated 100 sources from the complete set of blazars and pulsars for a test sample to calculate the accuracy of the classifier trained on the rest of the data set. This unitary test sample leads to an accuracy based on only that one test sample. In this way, the reported RF validation accuracy in that paper measures the same reliability as in

this paper, but with a more restricted approach to selecting a test sample.

2.5. Unassociated Sample

We conducted an initial investigation of our sample by combining gamma-ray properties from the 3FGL catalog for the 184 unassociated sources with the X-ray properties derived from the new spectral fits. Comparing the photometric and spectroscopic properties of the unassociated sample with those of the known pulsars and blazars, the unassociated sources tend to have lower gamma-ray fluxes than both the known blazars and pulsars. The mean X-ray fluxes of the unassociated counterparts fall between the mean fluxes of the known blazars and known pulsars.

The histograms in [Figure 2](#) show that the unassociated sources most readily overlap with the known blazar sample, suggesting that the majority of the unassociated sources should be blazars, consistent with the membership of known 3FGL sources. Interestingly, the histogram for X-ray photon index (the plot in the upper-left corner of [Figure 2](#)) shows two distinct peaks in the known 3FGL blazar distribution, with the unassociated source distribution overlapping primarily with the higher/softer peak.

Our model incorporating hydrogen-extincted power law spectra returned unusually high or low Γ_X for seven sources, as described above and listed in [Table 1](#). Given that some of these excesses also coincided with catalogued stars, we view these sources as dubious and do not include these seven sources in the ML classification.

3. RESULTS

Our X-ray spectral fits and RF classification results for the entire 3FGL unassociated catalog is available at CDS via anonymous ftp to [cdsarc.u-strasbg.fr](ftp://cdsarc.u-strasbg.fr) (130.79.128.5) or via <http://cdsarc.u-strasbg.fr/viz-bin/qcat?J/AJ>

The vast majority of examined X-ray excesses obtained well-defined spectral fits, reported in [Table 3](#). Most of the fits to the X-ray spectra have photon indices between 0 and 4, a similar range to the lists of known pulsars and blazars used to train the RF routine (as in [Figure 2](#)). This supports our first assumption that most of the unassociated sources are pulsars or blazars. These fits represent a large collection of X-ray parameters for likely counterparts to previously unassociated 3FGL gamma-ray sources. Five excesses had very few X-ray photons after summing up the *Swift*-XRT observations. With so few photons, the `xspec` fitting routine could not return useful spectral fits. For these spectra, we assumed $\Gamma_X = 2$ to calculate the flux.

The importances of the different parameters in the RF classifier indicate the features of the gamma- and X-ray

Table 2. RF feature importance

Γ_X	Γ_γ	Curvature	Variability index	$\log F_\gamma$	$\log F_X/F_\gamma$
0.033	0.097	0.41	0.13	0.08	0.25

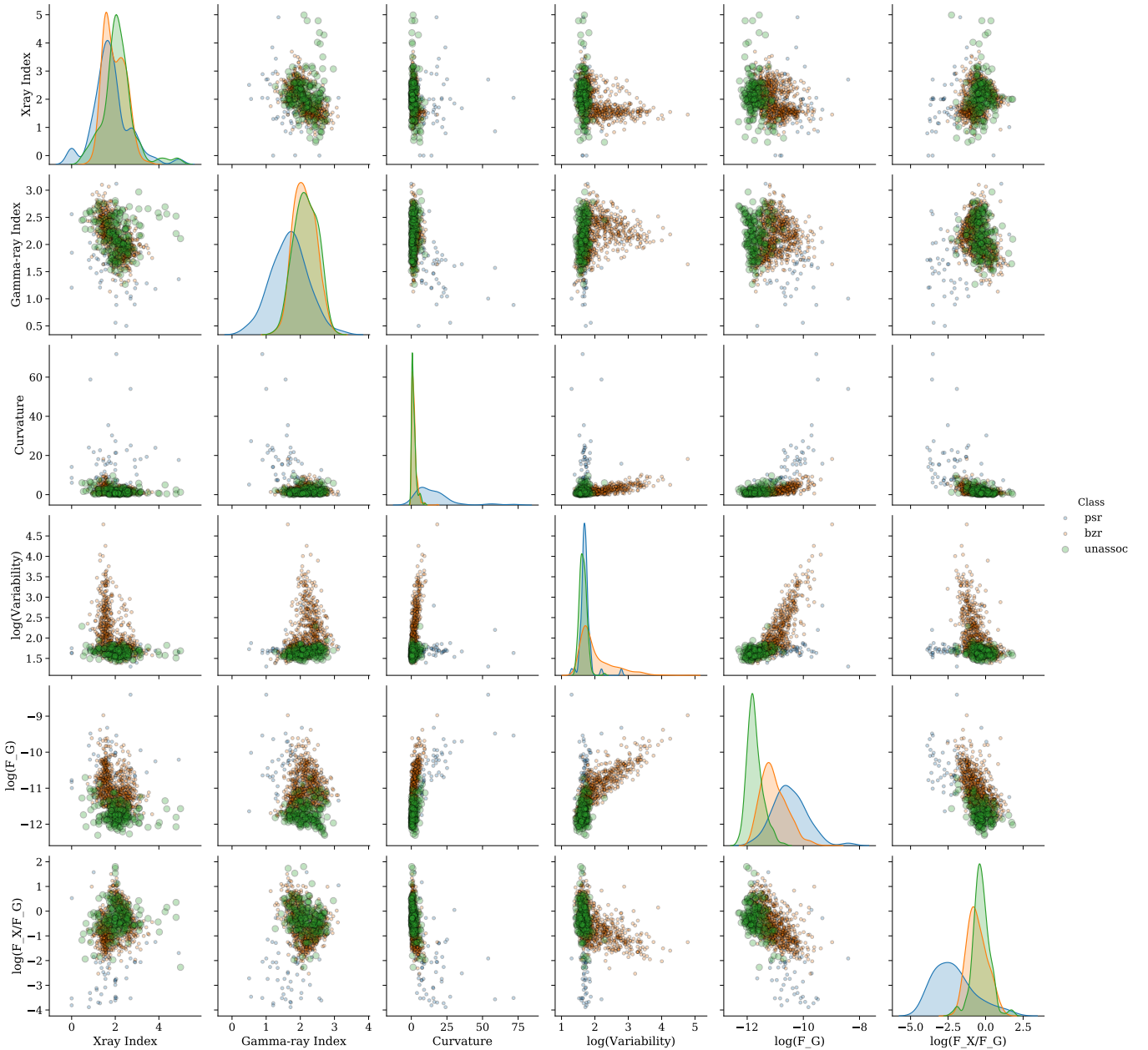


Figure 2. A full pairs plot of the known blazars (red), known pulsars (blue) and the unassociated sources (green). Histograms in the diagonal plots are smoothed and normalized to different scales for each class. The six parameters are the X-ray photon index, the gamma-ray photon index, the gamma-ray curvature index, the logarithm of the variability index, the logarithm of the gamma-ray flux in erg/s/cm^2 , and the logarithm of the ratio of X-ray to gamma-ray flux

spectra that are the strongest predictors of blazar or pulsar identification. The two most important features are gamma-ray spectral curvature and $\log F_X/F_\gamma$, shown in Table 2. Figure 1 shows that full X-ray fitting with both flux and photon index as free parameters did not alter X-ray flux by more than an order of magnitude for the vast majority of spectra. Some excesses did see a change in X-ray flux by around a half an order of magnitude; these spectra also showed the largest alterations in fitted photon index from $\Gamma_X \sim 2$. By this measure, fully fitting X-ray spectra instead of assuming $\Gamma_X = 2$ can correct reported X-ray flux by up to an order of magnitude and obtain photon index as a fitted parameter.

Applying the optimized RF classifier to the 177 fitted unassociated sources and X-ray excesses (ignoring the seven troublesome spectra discussed above), we use cross-validated blazar probabilities to categorize the unassociated sources. In this way, we use each of the ten subfolds used to validate the RF accuracy and average the blazar probability of each source from each fold. We identified 5 likely pulsars ($P_{bar} \leq 10\%$) and 126 likely blazars ($P_{bar} \geq 90\%$), with 46 sources remaining ambiguous. The results from this classification are reported in Table 4.

Figure 3 compares the blazar probability for the RF classification in this work to the same in Kaur et al. (2019) for the 161 sources analyzed in both works, color-coding the points by the fully fitted X-ray photon index. While the validation accuracy of the new RF classifier is not significantly different from the approach in Kaur et al. (2019), we have refined the blazar and pulsar catalogs and introduced new spectral information to all sources by fully fitting for photon index and X-ray flux. These alterations suggest that the new $P_{b_{zr}}$ values are more reliable than previous versions, facilitating the direct comparison in Figure 3.

In general, the addition of fully-fitted X-ray indices and fluxes to the ML training and test data sets did not alter the RF classifications for most of the 3FGL unassociated sources, and there is no pattern linking severe alterations in flux or photon index to previous estimates with drastically changed blazar probabilities. The most significant change in classifications were 13 sources previously classified as likely blazars and 3 previously classified as likely pulsars but here were labeled as ambiguous. Additionally, 7 ambiguous classifications in that previous work were here labeled as likely blazars. 138 of the 161 shared sources were sorted into the same category in both approaches.

We did not see any systematic relation that could be attributed as arising from a one-to-one relationship between altered X-ray photon index and changes in $P_{b_{zr}}$.

While many sources were classified with a similar blazar probability in this work and in (Kaur et al. 2019), some were classified as blazars or pulsars with greater confidence with more comprehensive spectral fits. Figure 3 shows that changes in blazar probability from (Kaur et al. 2019) to this work occur independently of divergence from coarse estimated spectral parameters. However, there are three overarching trends diverging from a one-to-one correspondence in the blazar probabilities shown in figure 3. Some likely blazars became ambiguous (or vice versa), and there is a general shift among previously more ambiguous sources towards higher blazar probabilities. That only ambiguous sources saw large systematic shifts towards higher blazar probabilities is reassurance that the addition of more comprehensive X-ray spectral fits adds valuable information for discriminating pulsars and blazars.

The locations of the X-ray counterparts in galactic coordinates are shown in Figure 4. While the counterparts classified as likely blazars and ambiguous are scattered roughly uniformly across the sky, the excesses with photon indices very different from expected for pulsars or blazars are almost entirely restricted to the galactic plane, which could be an indication that the X-rays of these excesses may be of galactic origin. If all the unusual excesses originate in similar astronomical objects, a catalog of gamma- and X-ray parameters of such objects could be used to add additional class to an RF scheme. As we do not know of a unified explanation for those excesses and as there is no previous catalogue of known similar objects it is not feasible to include sources of this unusual character as a class in the RF classifier method.

4. DISCUSSION AND CONCLUSIONS

In this work, we conducted full X-ray spectral analysis of counterparts to 3FGL unassociated sources, obtaining fluxes and photon indices for most of the X-ray sources examined. The vast majority of the X-ray sources linked to the 3FGL catalog unassociated sources were ably fit by our model, and represent a significant survey of dim excesses in the X-ray sky. Comprehensive X-ray spectral fits and the exclusion of unsuitable spectra together increase confidence in the output of the ML classification.

After training the RF classifier, the feature importances show in Table 2 show that $\log(F_X/F_G)$ was heavily weighted compared to most other parameters in the ML process, indicating that the ratio is an important discriminator for discerning blazars from pulsars. With previous estimates for X-ray flux differing from fully-fit fluxes by a factor of two or more, full X-ray spectral

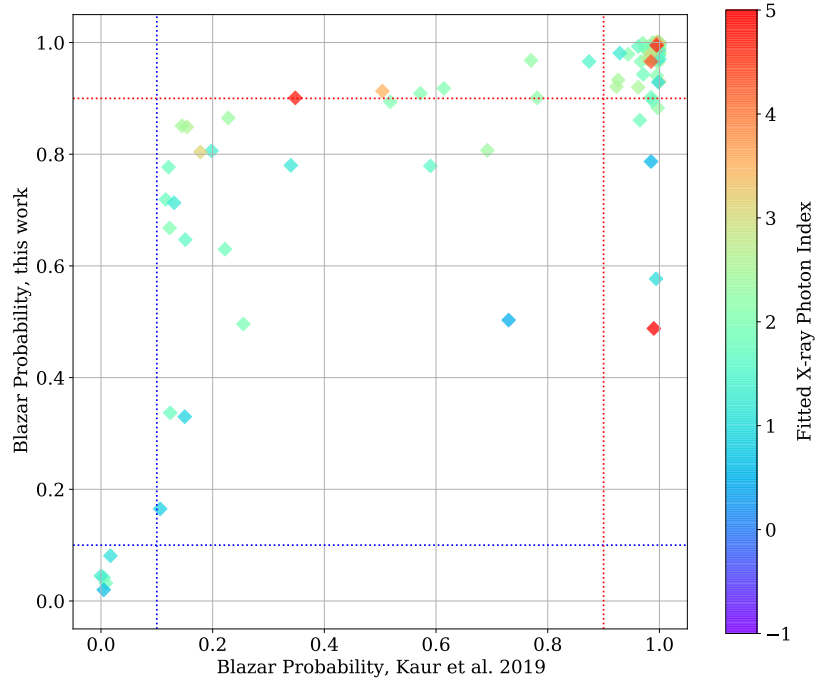


Figure 3. Blazar probability in this work vs in Kaur et al. (2019) for excesses analyzed in both works. Dotted red and blue vertical and horizontal lines show $< 10\%$ (likely pulsar) and $> 90\%$ (likely blazar) categorization bounds respectively. Points are color-coded by fully fitted X-ray photon indices with the same scale as figure 1

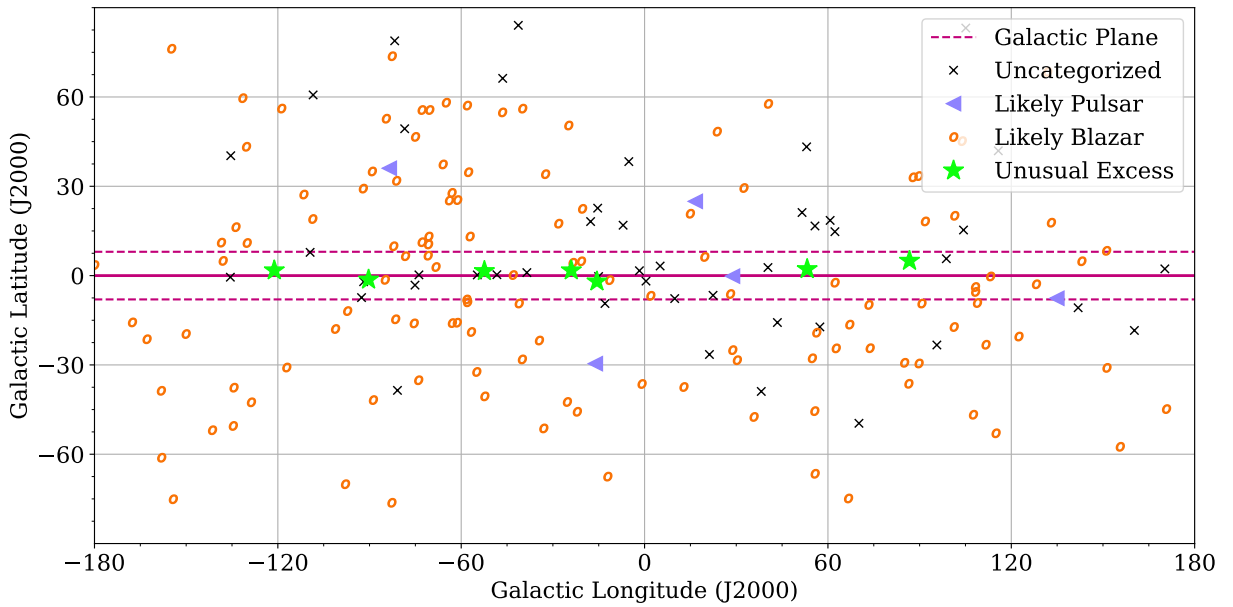


Figure 4. Galactic coordinates for the 184 X-ray counterparts examined in this work. Points include likely blazars, likely pulsars, and ambiguous counterparts, as well as the seven sources with unusual spectral fits. The galactic plane is approximately within the purple boundaries, and the galactic center is at $(l, b) = (0, 0)$.

analysis is an important contribution to ML classification of pulsars and blazars and to cataloging unassociated source X-ray parameters.

Finally, we compared our classification results to those obtained in previous work and found that introducing fully fit X-ray parameters achieves the same RF classification accuracy (98.5% in this work) as in Kaur et al. (2019) (99%) where the X-ray flux was obtained by assuming $\Gamma_X = 2$. The new approach with full X-ray fitting essentially matches the validation accuracy of the fixed photon index approach in Kaur et al. (2019), fulfilling our goal of meeting the old validation accuracy as a target. 138 of the 161 sources examine in both investigations were classified similarly. Including full X-ray spectral parameters shifts some sources into or out of the “likely blazar” category and shifts previously ambiguous sources to higher blazar probability.

Figure 3 shows a general increase in blazar probability for previously ambiguous sources, while likely pulsars did not see an increase in blazar probability. Given that many of the ambiguous sources are probably blazars, this trend suggests that the addition of X-ray spectral fits adds valuable information for discerning pulsars from blazars even if the changes are not dramatic enough to shift sources to 100% blazar probability.

In conducting full X-ray fitting, we discovered several clearly spurious X-ray sources. The elimination of these excesses from consideration is an important step in ensuring a reliable classification method, as those excesses would otherwise remain in consideration for classification as blazars or pulsars. By identifying possible stellar or instrumental origins for seven sources with X-ray photon indices $\Gamma_X < -1$ or $\Gamma_X > 5$, we showed that X-ray fitting can also sift out excesses that should not be immediately classified into blazars or pulsars via ML, further increasing the reliability of our results.

Besides a few sources identified as optical loading contaminants due to nearby bright stars, we selected seven spectra with X-ray photon indices significantly divergent from typical theoretical predictions of pulsars and blazars for further investigation. Because these sources are largely contained within the galactic plane, it is likely that they originate within the Milky Way. That six of the seven have a star within a few arcseconds suggests that some of these excesses may be linked to stellar phenomena and may be interesting targets for future investigations. Alternatively, the nearby stars in these seven cases may have been simple coincidences that are unrelated to the X-ray or gamma-ray source. In one of the seven cases, the stars may be contributing some optical loading in the *Swift*-XRT CCD, but for this $m_V = 9.2$ star, the optical loading contribution is

expected to be a small fraction relative to the detected X-ray count rate.

Though the requirements for X-ray fits create more stringent observational requirements in a multiwavelength ML routine compared to using only gamma-ray observations, incorporating diverse observations increases the comprehensive capabilities of the ML routine. Assuming $\Gamma_X = 2$ to obtain X-ray flux admitted to the ML analysis spectra that now are revealed to be poorly described by a blazar or pulsar model. These spectra might not actually be pulsars and blazars, but in assuming an X-ray photon index they might be incorrectly categorized. These unusual sources can be examined individually instead of analyzed automatically, allowing for more specialized future studies.

Even more comprehensive classification could be achieved by including X-ray variability measurements or expanding analysis into the ultraviolet bands using the UVOT telescope onboard *Swift* (Roming et al. 2005). Analysis of lower-energy photons together with X-ray and gamma-ray photons could also constrain the location of the synchrotron peak in each spectrum, greatly increasing the detail in the characterization of the source. It will be particularly interesting to apply a growing understanding of pulsar and blazar classification to the results of surveys using new and upcoming space telescopes such as eROSITA. Whether the characteristics of bright pulsars and blazars are similar to those of dimmer pulsars and blazars should become evident as wide-field surveys extend to dimmer magnitudes.

Eventually, after the easier to find blazars and pulsars have been identified, it may become prudent to expand ML classification beyond a binary choice of pulsars and blazars. To that end, switching from a RF routine to a more detailed approach such as guided clustering would dramatically increase the flexibility of the automated system at the cost of more strenuous supervision requirements.

ACKNOWLEDGEMENTS

We are grateful to the reviewer for their insightful and detailed commentary, which was vital in improving and focusing this work.

This research has made use of data and/or software provided by the High Energy Astrophysics Science Archive Research Center (HEASARC), which is a service of the Astrophysics Science Division at NASA/GSFC. The authors gratefully acknowledge the support of NASA grants 80NSSC17K0752 and 80NSSC18K1730.

Michael C. Stroh is partially supported by the Heising-Simons Foundation under grant 2018-0911.

CATALOG

The machine-readable tables corresponding to Tables 3 and 4 are available at CDS via anonymous

ftp to [cdsarc.u-strasbg.fr](ftp://cdsarc.u-strasbg.fr) (130.79.128.5) or via <http://cdsarc.u-strasbg.fr/viz-bin/qcat?J/AJ>.

Additional thanks is due to the CDS and VizieR teams for facilitating this web service.

REFERENCES

- Abdo, A. A., Ajello, M., Allafort, A., et al. 2013, *ApJS*, 208, 17, doi: [10.1088/0067-0049/208/2/17](https://doi.org/10.1088/0067-0049/208/2/17)
- Acerro, F., Ackermann, M., Ajello, M., et al. 2015, *Astrophysical Journal, Supplement Series*, 218, doi: [10.1088/0067-0049/218/2/23](https://doi.org/10.1088/0067-0049/218/2/23)
- Ackermann, M., Ajello, M., Atwood, W. B., et al. 2015, *Astrophysical Journal*, 810, doi: [10.1088/0004-637X/810/1/14](https://doi.org/10.1088/0004-637X/810/1/14)
- Arnaud, K. A. 1996, *ASP Conference Series*, 101
- Breiman, L. 2001, 45, 5
- Burrows, D. N., Hill, J. E., Nousek, J. A., et al. 2005, *SSRv*, 120, 165, doi: [10.1007/s11214-005-5097-2](https://doi.org/10.1007/s11214-005-5097-2)
- Cash, W. 1976, *Astronomy & Astrophysics*, 52, 307
- Chawla, N. V., Bowyer, K. W., Hall, L. O., & Kegelmeyer, W. P. 2002, *Journal of Artificial Intelligence Research*, 16, 321
- Evans, P. A., Page, K. L., Osborne, J. P., et al. 2020, *The Astrophysical Journal Supplement Series*, 247, 54, doi: [10.3847/1538-4365/ab7db9](https://doi.org/10.3847/1538-4365/ab7db9)
- Ferrara, E. C., Mirabal, N. R., & Fermi-LAT Collaboration. 2015, in *American Astronomical Society Meeting Abstracts*, Vol. 225, American Astronomical Society Meeting Abstracts #225, 336.02
- Fossati, G., Maraschi, L., Celotti, A., Comastri, A., & Ghisellini, G. 1998, *MNRAS*, 299, 433, doi: [10.1046/j.1365-8711.1998.01828.x](https://doi.org/10.1046/j.1365-8711.1998.01828.x)
- Gehrels, N., Chincarini, G., Giommi, P., et al. 2004, *ApJ*, 611, 1005, doi: [10.1086/422091](https://doi.org/10.1086/422091)
- Ghisellini, G., Righi, C., Costamante, L., & Tavecchio, F. 2017, doi: [10.1093/mnras/stx806](https://doi.org/10.1093/mnras/stx806)
- Hassan, T., Mirabal, N., Contreras, J. L., & Oya, I. 2012, *Monthly Notices of the Royal Astronomical Society*, 428, 220, doi: [10.1093/mnras/sts022](https://doi.org/10.1093/mnras/sts022)
- Kaur, A., Falcone, A. D., Stroh, M. D., Kennea, J. A., & Ferrara, E. C. 2019, doi: [10.3847/1538-4357/ab4ceb](https://doi.org/10.3847/1538-4357/ab4ceb)
- Last, F., Douzas, G., & Bacao, F. 2017, arXiv e-prints, arXiv:1711.00837. <https://arxiv.org/abs/1711.00837>
- Li, K.-L., Hou, X., Strader, J., et al. 2018, *ApJ*, 863, 194, doi: [10.3847/1538-4357/aad243](https://doi.org/10.3847/1538-4357/aad243)
- Marelli, M. 2012, arXiv e-prints, arXiv:1205.1748. <https://arxiv.org/abs/1205.1748>
- McFadden, R., Karastergiou, A., & Roberts, S. 2017, *Proceedings of the International Astronomical Union*, 13, 372–373, doi: [10.1017/S1743921317009000](https://doi.org/10.1017/S1743921317009000)
- Roming, P. W. A., Kennedy, T. E., Mason, K. O., et al. 2005, *SSRv*, 120, 95, doi: [10.1007/s11214-005-5095-4](https://doi.org/10.1007/s11214-005-5095-4)
- Saz Parkinson, P. M., Xu, H., Yu, P. L. H., et al. 2016, *ApJ*, 820, 8, doi: [10.3847/0004-637X/820/1/8](https://doi.org/10.3847/0004-637X/820/1/8)
- Wilms, J., Allen, A., & McCray, R. 2000, *Astrophysical Journal*, 542, 914
- Wu, J., Clark, C. J., Pletsch, H. J., et al. 2018, *ApJ*, 854, 99, doi: [10.3847/1538-4357/aaa411](https://doi.org/10.3847/1538-4357/aaa411)
- Zyuzin, D. A., Karpova, A. V., & Shibanov, Y. A. 2018, *MNRAS*, 476, 2177, doi: [10.1093/mnras/sty359](https://doi.org/10.1093/mnras/sty359)

Table 3. X-ray photon indices and fluxes (0.3 – 10.0 keV) for the 184 X-ray excesses matched with 3FGL unassociated sources used in this paper, including the five spectra unable to be fit by Xspec (marked with dashes) and the seven excluded spectra (**boldface**). Certain spectra were unable to have asymmetric errors for Γ_X ; these results use the default symmetric error and are marked with an asterisk (*). Available at CDS via anonymous ftp to cdsarc.u-strasbg.fr (130.79.128.5) or via <http://cdsarc.u-strasbg.fr/viz-bin/qcat?J/AJ>

<i>Swift</i> X-ray excess	3FGL gamma-ray source	Γ_X	$\log_{10} F_X$	Cstat	DOF
SwF3	3FGL		erg/s/cm ²		
J000805.3+145018	J0008.3+1456	1.60 ^{0.15} _{0.14}	-11.17 ^{+0.06} _{-0.05}	82.17	89
J003159.9+093615	J0031.6+0938	2.11 ^{0.51} _{0.52}	-12.41 ^{+0.17} _{-0.13}	7.73	15
J004859.5+422348	J0049.0+4224	2.24 ^{0.38} _{0.39}	-12.19 ^{+0.09} _{-0.08}	33.91	34
J012152.5-391544	J0121.8-3917	1.81 ^{0.08} _{0.08}	-11.45 ^{+0.03} _{-0.03}	174.26	198
J013255.1+593213	J0133.3+5930	2.16 ^{0.24} _{0.23}	-11.85 ^{+0.06} _{-0.06}	51.59	57
J015624.4-242003	J0156.5-2423	2.30 ^{0.14} _{0.14}	-11.90 ^{+0.04} _{-0.04}	79.58	93
J015852.4+010126	J0158.6+0102	1.82 ^{0.82} _{0.73}	-12.54 ^{+0.16} _{-0.17}	4.09	6
J020020.9-410933	J0200.3-4108	2.66 ^{0.24} _{0.24}	-12.19 ^{+0.06} _{-0.06}	34.45	44
J021210.6+532139	J0212.1+5320	1.06 ^{0.14} _{0.14}	-11.82 ^{+0.05} _{-0.05}	73.84	110
J023854.1+255405	J0239.0+2555	2.17 ^{0.15} _{0.14}	-11.83 ^{+0.04} _{-0.04}	79.87	93
J024454.9+475117	J0244.4+4745	2.33 ^{0.50} _{0.50}	-12.68 ^{+0.10} _{-0.11}	14.22	14
J025111.4-183115	J0251.1-1829	2.01 ^{0.16} _{0.15}	-12.20 ^{+0.05} _{-0.05}	68.54	82
J025857.4+055243	J0258.9+0552	1.97 ^{0.30} _{0.29}	-12.22 ^{+0.08} _{-0.08}	23.23	31
J034050.0-242259	J0340.4-2423	2.27 ^{0.30} _{0.30}	-12.50 ^{+0.09} _{-0.09}	18.24	27
J034158.1+314851	J0342.3+3148c	1.22 ^{0.16} _{0.16}	-11.59 ^{+0.05} _{-0.05}	90	97
J034819.8+603506	J0348.4+6039	1.42 ^{0.36} _{0.36}	-11.09 ^{+0.09} _{-0.09}	28.53	25
J035051.2-281632	J0351.0-2816	1.94 ^{0.06} _{0.06}	-11.49 ^{+0.02} _{-0.02}	235.76	239
J035939.3+764627	J0359.7+7649	3.10 ^{0.80} _{0.79}	-12.13 ^{+0.21} _{-0.18}	3.20	7
J041433.2-084213	J0414.9-0840	2.12 ^{0.38} _{0.39}	-12.66 ^{+0.13} _{-0.10}	21.33	25
J042011.0-601504	J0420.4-6013	2.15 ^{0.10} _{0.10}	-11.69 ^{+0.03} _{-0.03}	117.35	146
J042749.8-670434*	J0427.9-6704	-0.15 ^{0.19} _{0.19}	-11.78 ^{+0.06} _{-0.06}	93.03	101
J042958.7-305931	J0430.1-3103	2.67 ^{0.24} _{0.24}	-12.19 ^{+0.06} _{-0.06}	41.66	42
J043836.9-732919	J0437.7-7330	2.08 ^{0.29} _{0.29}	-12.39 ^{+0.08} _{-0.09}	36.58	26
J044722.5-253937	J0447.1-2540	4.02 ^{0.93} _{0.75}	-12.80 ^{+0.15} _{-0.16}	4.52	8
J045149.6+572140	J0451.7+5722	2.82 ^{0.57} _{0.50}	-12.42 ^{+0.18} _{-0.15}	17.11	14
J050650.1+032359	J0506.9+0321	2.61 ^{0.14} _{0.13}	-12.24 ^{+0.03} _{-0.03}	96.36	117
J051641.4+101243	J0516.6+1012	2.32 ^{0.35} _{0.34}	-12.40 ^{+0.08} _{-0.08}	25.04	28
J052939.5+382321	J0529.2+3822	1.75 ^{0.46} _{0.45}	-12.19 ^{+0.09} _{-0.09}	27.12	24
J053357.3-375754	J0533.8-3754	2.50 ^{0.61} _{0.58}	-12.39 ^{+0.13} _{-0.15}	3.40	8
J053559.3-061624	J0535.7-0617c	2.58 ^{0.32} _{0.32}	-11.95 ^{+0.07} _{-0.07}	28.41	34
J055940.6+304232	J0559.8+3042	1.92 ^{0.81} _{0.83}	-12.36 ^{+0.22} _{-0.12}	6.97	14
J070421.7-482645	J0704.3-4828	2.49 ^{0.15} _{0.14}	-12.01 ^{+0.04} _{-0.04}	78.40	99
J071046.2-102942	J0711.1-1037	1.04 ^{0.34} _{0.34}	-11.73 ^{+0.10} _{-0.09}	33.45	39

Table 3 continued

Table 3 (*continued*)

<i>Swift</i> X-ray excess	3FGL gamma-ray source	Γ_X	$\log_{10} F_X$	Cstat	DOF
SwF3	3FGL		erg/s/cm ²		
J072547.5–054830	J0725.7–0550	2.35 $^{0.16}_{0.16}$	–11.63 $^{+0.04}_{-0.04}$	91.01	105
J074626.10–022551	J0746.4–0225	2.41 $^{0.17}_{0.17}$	–11.87 $^{+0.04}_{-0.05}$	76.14	79
J074724.8–492633	J0747.5–4927	2.46 $^{0.22}_{0.21}$	–11.97 $^{+0.05}_{-0.05}$	55.18	56
J074903.8–221015	J0748.8–2208	6.29 $^{1.86}_{1.76}$	–10.59 $^{+0.80}_{-0.77}$	4	4
J080215.8–094214	J0802.3–0941	2.44 $^{0.24}_{0.23}$	–12.20 $^{+0.06}_{-0.06}$	32.19	43
J081338.1–035717	J0813.5–0356	1.80 $^{0.12}_{0.12}$	–11.49 $^{+0.04}_{-0.04}$	142.84	125
J082623.6–505742	J0826.3–5056	1.35 $^{0.32}_{0.31}$	–12.27 $^{+0.09}_{-0.09}$	26.19	33
J082628.2–640415	J0826.3–6400	2.09 $^{0.05}_{0.05}$	–10.75 $^{+0.01}_{-0.01}$	312.05	327
J083843.4–282701	J0838.8–2829	1.75 $^{0.04}_{0.04}$	–11.25 $^{+0.01}_{-0.01}$	374.75	464
J084831.8–694108	J0847.2–6936	1.90 $^{0.21}_{0.21}$	–12.18 $^{+0.06}_{-0.06}$	67.42	66
J085505.8–481517	J0855.4–4818	– – ± – –	– – – –	–	–
J090530.4–491840	J0905.6–4917	7.84 $^{0.51}_{0.50}$	–8.99 $^{+0.23}_{-0.23}$	40.38	38
J091926.1–220043	J0919.5–2200	2.05 $^{0.20}_{0.20}$	–12.49 $^{+0.06}_{-0.06}$	48.26	52
J092818.4–525659	J0928.3–5255	2.98 $^{0.63}_{0.57}$	–11.47 $^{+0.33}_{-0.24}$	25.91	19
J093444.6+090355	J0935.2+0903	2.40 $^{0.79}_{0.81}$	–12.34 $^{+0.22}_{-0.17}$	7.13	6
J093754.6–143349	J0937.9–1435	2.42 $^{0.36}_{0.35}$	–12.53 $^{+0.08}_{-0.09}$	16.12	24
J095249.5+071329	J0952.8+0711	1.98 $^{0.24}_{0.23}$	–12.16 $^{+0.08}_{-0.08}$	38.43	37
J101545.9–602938	J1016.5–6034	3.08 $^{0.23}_{0.21}$	–11.54 $^{+0.09}_{-0.08}$	146.34	104
J102432.6–454428	J1024.4–4545	2.35 $^{0.12}_{0.11}$	–11.51 $^{+0.03}_{-0.03}$	112.07	145
J103332.4–503526	J1033.4–5035	2.28 $^{0.18}_{0.17}$	–11.75 $^{+0.04}_{-0.04}$	80.52	88
J103755.1–242546	J1038.0–2425	1.24 $^{0.26}_{0.27}$	–12.24 $^{+0.11}_{-0.11}$	34.05	31
J103831.1–581346	J1039.1–5809	4.28 $^{0.66}_{0.59}$	–11.38 $^{+0.36}_{-0.32}$	42.52	25
J104939.4+154839	J1049.7+1548	2.62 $^{0.17}_{0.17}$	–12.27 $^{+0.04}_{-0.04}$	68.58	73
J105224.5+081409	J1052.0+0816	1.90 $^{0.15}_{0.14}$	–11.62 $^{+0.05}_{-0.05}$	96.27	90
J110025.5–205333	J1100.2–2044	1.01 $^{0.66}_{0.79}$	–12.02 $^{+0.41}_{-0.30}$	14.86	11
J110224.1–773339	J1104.3–7736c	2.47 $^{0.09}_{0.10}$	–11.77 $^{+0.02}_{-0.02}$	192.57	145
J111601.8–484222	J1116.7–4854	2.18 $^{0.41}_{0.41}$	–12.58 $^{+0.08}_{-0.08}$	29.45	32
J111715.2–533815	J1117.2–5338	1.97 $^{0.31}_{0.32}$	–12.08 $^{+0.08}_{-0.08}$	28.25	35
J111956.10–264322	J1119.8–2647	1.98 $^{0.32}_{0.32}$	–12.35 $^{+0.10}_{-0.09}$	37.97	27
J111958.9–220456	J1119.9–2204	1.89 $^{0.18}_{0.17}$	–13.10 $^{+0.06}_{-0.06}$	78.43	82
J112042.4+071313	J1120.6+0713	1.76 $^{0.26}_{0.26}$	–12.54 $^{+0.09}_{-0.09}$	36.75	29
J112504.2–580539	J1125.1–5803	2.47 $^{0.26}_{0.25}$	–11.66 $^{+0.07}_{-0.07}$	40.45	52
J112624.8–500806	J1126.8–5001	1.67 $^{0.06}_{0.07}$	–11.84 $^{+0.02}_{-0.02}$	248.78	282
J113032.7–780107	J1130.7–7800	1.80 $^{0.05}_{0.05}$	–10.80 $^{+0.02}_{-0.02}$	312.78	326
J113209.3–473853	J1132.0–4736	1.68 $^{0.07}_{0.07}$	–11.17 $^{+0.02}_{-0.02}$	268.25	287
J114600.8–063851	J1146.1–0640	2.12 $^{0.22}_{0.22}$	–12.01 $^{+0.07}_{-0.06}$	49.95	51
J114911.10+280719	J1149.1+2815	4.05 $^{0.77}_{0.62}$	–12.47 $^{+0.16}_{-0.14}$	13.54	10
J115514.5–111125	J1155.3–1112	1.78 $^{0.38}_{0.38}$	–12.28 $^{+0.15}_{-0.13}$	27.06	26
J120055.1–143039	J1200.9–1432	1.76 $^{0.26}_{0.26}$	–12.09 $^{+0.09}_{-0.08}$	39.89	37
J121553.0–060940*	J1216.6–0557	1.50 $^{2.12}_{2.12}$	–12.37 $^{+16.37}_{-\infty}$	0	0

Table 3 *continued*

Table 3 (*continued*)

<i>Swift</i> X-ray excess	3FGL gamma-ray source	Γ_X	$\log_{10} F_X$	Cstat	DOF
SwF3	3FGL		erg/s/cm ²		
J122014.4–245948	J1220.0–2502	1.93 ^{0.11} _{0.11}	–11.54 ^{+0.03} _{–0.03}	114.51	151
J122019.8–371414	J1220.1–3715	2.05 ^{0.17} _{0.17}	–11.78 ^{+0.05} _{–0.05}	78.36	72
J122127.4–062845	J1221.5–0632	1.89 ^{0.17} _{0.16}	–12.54 ^{+0.06} _{–0.06}	58.62	73
J122257.0+121438	J1223.2+1215	1.89 ^{0.31} _{0.30}	–13.09 ^{+0.10} _{–0.10}	31.83	31
J122536.7–344723	J1225.4–3448	2.14 ^{0.10} _{0.10}	–11.52 ^{+0.03} _{–0.03}	116.66	154
J123140.3+482148	J1231.6+4825	1.97 ^{0.62} _{0.64}	–12.38 ^{+0.25} _{–0.16}	16.77	13
J123204.2+165527	J1232.3+1701	– – ± – –	– – – –	–	–
J123235.9–372055	J1232.5–3720	2.40 ^{0.35} _{0.33}	–12.40 ^{+0.09} _{–0.09}	11.07	20
J123447.7–043253	J1234.7–0437	2.13 ^{0.39} _{0.38}	–12.58 ^{+0.12} _{–0.12}	19.29	16
J123726.6–705140	J1236.6–7050	1.67 ^{0.43} _{0.43}	–12.20 ^{+0.13} _{–0.11}	21.67	20
J124021.3–714858	J1240.3–7149	1.87 ^{0.05} _{0.05}	–10.81 ^{+0.01} _{–0.01}	310.77	370
J124919.5–280833	J1249.1–2808	2.08 ^{0.07} _{0.07}	–11.46 ^{+0.02} _{–0.02}	189.35	236
J124919.7–054540	J1249.5–0546	2.91 ^{0.31} _{0.30}	–12.52 ^{+0.07} _{–0.08}	20.84	31
J125058.4–494444	J1251.0–4943	2.32 ^{0.45} _{0.42}	–12.52 ^{+0.09} _{–0.10}	22.31	18
J125821.5+212351	J1258.4+2123	2.33 ^{0.21} _{0.21}	–12.22 ^{+0.06} _{–0.06}	43.69	48
J130059.5–814809	J1259.3–8151	1.29 ^{0.46} _{0.46}	–12.31 ^{+0.17} _{–0.15}	19.12	15
J130128.9+333711	J1301.5+3333	1.59 ^{0.40} _{0.40}	–12.68 ^{+0.16} _{–0.15}	17.50	16
J130832.0+034406	J1309.0+0347	1.59 ^{0.28} _{0.27}	–12.13 ^{+0.11} _{–0.11}	27.09	30
J131140.3–623313*	J1311.8–6230	1.02 ^{1.51} _{1.51}	–12.85 ^{+0.40} _{–0.34}	1.84	2
J131552.8–073304	J1315.7–0732	2.37 ^{0.10} _{0.10}	–11.64 ^{+0.03} _{–0.03}	118.98	144
J132928.6–053135	J1329.1–0536	1.83 ^{0.13} _{0.13}	–11.60 ^{+0.05} _{–0.05}	92.98	98
J132939.6–610735	J1329.8–6109	6.22 ^{0.54} _{0.59}	–10.83 ^{+0.23} _{–0.26}	26.73	22
J140514.7–611822	J1405.4–6119	–0.12 ^{0.37} _{0.38}	–12.10 ^{+0.05} _{–0.05}	129.53	128
J141045.2+740504	J1410.9+7406	2.59 ^{0.53} _{0.53}	–12.79 ^{+0.12} _{–0.11}	7.23	14
J141133.3–072256	J1411.4–0724	2.24 ^{0.26} _{0.25}	–12.25 ^{+0.07} _{–0.07}	30.32	35
J142035.9–243021	J1421.0–2431	4.79 ^{0.74} _{0.66}	–12.06 ^{+0.16} _{–0.16}	16.31	13
J144544.5–593200	J1445.7–5925	3.17 ^{1.07} _{0.96}	–11.20 ^{+0.63} _{–0.44}	5	5
J151150.10+662450	J1512.3+6622	1.74 ^{0.12} _{0.12}	–11.70 ^{+0.05} _{–0.04}	126.57	109
J151256.6–564027*	J1512.8–5639	–0.35 ^{0.47} _{0.47}	–11.70 ^{+0.12} _{–0.12}	34.73	28
J151319.0–372015	J1513.3–3719	2.81 ^{0.28} _{0.28}	–12.42 ^{+0.07} _{–0.07}	40.28	34
J151649.8+263635	J1517.0+2637	2.20 ^{0.43} _{0.41}	–12.59 ^{+0.10} _{–0.11}	16.68	16
J152603.0–083146	J1525.8–0834	– – ± – –	– – – –	–	–
J152818.2–290256	J1528.1–2904	1.72 ^{0.24} _{0.24}	–12.10 ^{+0.08} _{–0.08}	36.96	47
J154150.1+141441	J1541.6+1414	2.58 ^{0.44} _{0.37}	–12.53 ^{+0.10} _{–0.10}	18.66	18
J154343.6–255607	J1544.1–2555	3.10 ^{0.54} _{0.54}	–12.34 ^{+0.12} _{–0.11}	10.24	15
J154459.2–664147	J1545.0–6641	2.13 ^{0.06} _{0.06}	–11.01 ^{+0.02} _{–0.02}	269.72	300
J154946.4–304502	J1549.9–3044	2.24 ^{0.16} _{0.16}	–11.80 ^{+0.04} _{–0.04}	66.66	88
J161543.2–444921	J1615.6–4450	4.36 ^{0.42} _{0.44}	–11.42 ^{+0.15} _{–0.16}	44.98	23
J162432.2–465756	J1624.1–4700	7.42 ^{0.42} _{0.42}	–9.17 ^{+0.17} _{–0.18}	32.20	40
J162437.8–423144	J1624.8–4233	3.08 ^{0.65} _{0.53}	–12.09 ^{+0.22} _{–0.18}	27.59	14

Table 3 *continued*

Table 3 (*continued*)

<i>Swift</i> X-ray excess	3FGL gamma-ray source	Γ_X	$\log_{10} F_X$	Cstat	DOF
SwF3	3FGL		erg/s/cm ²		
J162607.8–242736	J1626.2–2428c	$0.87_{0.56}^{0.56}$	$-12.34_{-0.16}^{+0.17}$	8.14	12
J162743.0+322102	J1627.8+3217	$2.38_{0.19}^{0.20}$	$-12.47_{-0.06}^{+0.05}$	51.73	53
J165338.2–015837	J1653.6–0158	$1.29_{0.28}^{0.28}$	$-12.73_{-0.10}^{+0.10}$	38.62	37
J170409.6+123423	J1704.1+1234	$2.02_{0.09}^{0.10}$	$-11.50_{-0.03}^{+0.03}$	137.89	163
J170433.9–052840	J1704.4–0528	$1.91_{0.09}^{0.09}$	$-11.43_{-0.03}^{+0.03}$	144.39	197
J170521.6–413436	1710.6–4128c	– – ± – –	– – – –	–	–
J171106.10–432415	J1710.6–4317	$6.32_{0.43}^{0.42}$	$-10.26_{-0.18}^{+0.16}$	40.58	39
J172142.1–392204	J1721.8–3919	$1.08_{0.25}^{0.24}$	$-11.78_{-0.06}^{+0.06}$	63.43	65
J172858.2+604359	J1729.0+6049	$4.79_{1.42}^{1.55}$	$-11.72_{-0.45}^{+0.57}$	16.32	7
J173250.5+591233	J1732.7+5914	$2.14_{0.29}^{0.30}$	$-12.36_{-0.08}^{+0.08}$	20.59	28
J173508.1–292955	J1734.7–2930	$1.94_{0.40}^{0.41}$	$-11.91_{-0.09}^{+0.09}$	23.55	23
J174511.10–225455	J1744.7–2252	$0.88_{0.15}^{0.14}$	$-11.74_{-0.05}^{+0.05}$	111.59	129
J175316.4–444822	J1753.6–4447	$2.03_{0.41}^{0.40}$	$-12.58_{-0.10}^{+0.10}$	13.72	19
J175359.7–292909	J1754.0–2930	$0.83_{0.22}^{0.22}$	$-11.80_{-0.07}^{+0.07}$	71.97	74
J180351.7+252607	J1804.1+2532	$1.20_{0.34}^{0.35}$	$-12.39_{-0.12}^{+0.13}$	23.03	22
J180425.0–085002	J1804.5–0850	$1.48_{0.32}^{0.33}$	$-12.08_{-0.09}^{+0.09}$	23.34	31
J181307.6–684713	J1813.6–6845	$2.04_{0.46}^{0.46}$	$-12.95_{-0.12}^{+0.13}$	25.63	20
J181720.4–303257	J1817.3–3033	$1.86_{0.13}^{0.13}$	$-11.80_{-0.04}^{+0.04}$	108.11	129
J182914.0+272901	J1829.2+2731	$1.25_{0.19}^{0.19}$	$-12.10_{-0.07}^{+0.07}$	50.73	65
J182915.5+323432	J1829.2+3229	$2.46_{0.73}^{0.83}$	$-12.02_{-0.18}^{+0.22}$	4.32	6
J183659.5–240027	J1837.3–2403	$1.17_{1.04}^{0.93}$	$-13.28_{-0.27}^{+0.31}$	5.42	7
J184433.1–034627*	J1844.3–0344	$0.62_{0.64}^{0.64}$	$-12.64_{-0.11}^{+0.12}$	31.22	29
J184833.10+323249	J1848.6+3232	$0.47_{0.65}^{0.62}$	$-12.45_{-0.24}^{+0.25}$	10.01	8
J185520.0+075138	J1855.6+0753	$0.84_{0.40}^{0.40}$	$-12.12_{-0.10}^{+0.11}$	43.66	26
J185606.6–122147	J1856.1–1217	$2.06_{0.25}^{0.26}$	$-11.78_{-0.06}^{+0.05}$	45.45	52
J190444.5–070743	J1904.7–0708	$2.21_{0.34}^{0.35}$	$-12.23_{-0.09}^{+0.08}$	25.28	26
J192113.10+194004	J1921.6+1934	$6.19_{0.49}^{0.51}$	$-10.13_{-0.22}^{+0.22}$	41.87	30
J192242.1–745354	J1923.2–7452	$2.25_{0.09}^{0.09}$	$-11.44_{-0.03}^{+0.03}$	167.01	174
J193420.1+600138	J1934.2+6002	$2.51_{0.27}^{0.27}$	$-12.11_{-0.06}^{+0.06}$	33.01	45
J194633.6–540235	J1946.4–5403	$1.69_{0.24}^{0.24}$	$-12.68_{-0.09}^{+0.09}$	39.86	39
J195149.7+690719	J1951.3+6909	$2.65_{0.45}^{0.47}$	$-12.33_{-0.09}^{+0.09}$	16.30	19
J195800.3+243803	J1958.1+2436	$2.22_{0.31}^{0.31}$	$-11.43_{-0.07}^{+0.09}$	33.81	48
J200635.7+015222	J2006.6+0150	$1.82_{0.32}^{0.32}$	$-12.40_{-0.10}^{+0.11}$	28.78	22
J201020.3–212434	J2010.0–2120	$1.50_{0.52}^{0.50}$	$-12.14_{-0.18}^{+0.21}$	14.71	11
J201525.3–143204	J2015.3–1431	$3.15_{0.34}^{0.35}$	$-12.28_{-0.08}^{+0.08}$	19.68	28
J203027.9–143919	J2030.5–1439	$1.51_{0.30}^{0.32}$	$-12.19_{-0.12}^{+0.12}$	21.77	31
J203450.9–420038	J2034.6–4202	$2.59_{0.12}^{0.12}$	$-11.84_{-0.03}^{+0.03}$	108.50	121
J203556.9+490038	J2035.8+4902	$5.82_{0.63}^{0.61}$	$-10.70_{-0.26}^{+0.24}$	21.96	21
J203935.8+123001	J2039.7+1237	– – ± – –	– – – –	–	–
J204351.5+103407	J2044.0+1035	$2.51_{0.33}^{0.33}$	$-12.34_{-0.08}^{+0.08}$	21.71	28

Table 3 *continued*

Table 3 (*continued*)

<i>Swift</i> X-ray excess	3FGL gamma-ray source	Γ_X	$\log_{10} F_X$	Cstat	DOF
SwF3	3FGL		erg/s/cm ²		
J204806.3–312011	J2047.9–3119	2.21 ^{0.28} _{0.28}	–12.23 ^{+0.07} _{–0.07}	28.19	38
J205350.8+292312	J2053.9+2922	2.24 ^{0.09} _{0.09}	–10.93 ^{+0.02} _{–0.02}	191.26	194
J205357.9+690517	J2054.3+6907	0.54 ^{0.31} _{0.32}	–12.66 ^{+0.11} _{–0.12}	38.95	32
J205950.4+202905	J2059.9+2029	2.22 ^{0.35} _{0.34}	–12.28 ^{+0.08} _{–0.09}	26.63	23
J210940.0+043958	J2110.0+0442	1.99 ^{0.25} _{0.24}	–11.94 ^{+0.07} _{–0.07}	36.05	39
J211522.2+121801	J2115.2+1215	3.18 ^{0.47} _{0.45}	–12.38 ^{+0.12} _{–0.11}	8.35	18
J212051.6–125300	J2120.4–1256	0.66 ^{0.39} _{0.41}	–12.57 ^{+0.16} _{–0.16}	7.79	17
J212601.5+583148	J2125.8+5832	1.81 ^{0.36} _{0.35}	–12.08 ^{+0.08} _{–0.08}	35.73	26
J212729.3–600102	J2127.5–6001	1.24 ^{0.15} _{0.13}	–11.48 ^{+0.05} _{–0.06}	131.95	94
J214247.5+195811	J2142.7+1957	2.38 ^{0.22} _{0.22}	–11.83 ^{+0.05} _{–0.05}	64.31	60
J214429.5–563849	J2144.6–5640	2.04 ^{0.25} _{0.24}	–12.27 ^{+0.08} _{–0.08}	35.85	38
J215046.5–174956	J2150.5–1754	3.50 ^{1.06} _{0.75}	–12.38 ^{+0.19} _{–0.16}	13.51	9
J215122.10+415634	J2151.6+4154	2.58 ^{0.24} _{0.23}	–11.61 ^{+0.06} _{–0.06}	42.19	63
J220941.4–045108	J2209.8–0450	2.46 ^{0.49} _{0.51}	–12.53 ^{+0.10} _{–0.11}	12.92	13
J222911.2+225456	J2229.1+2255	2.14 ^{0.07} _{0.07}	–11.24 ^{+0.02} _{–0.02}	191.20	215
J224437.0+250344	J2244.6+2503	2.87 ^{0.36} _{0.34}	–12.42 ^{+0.08} _{–0.09}	39.92	24
J224710.1–000512*	J2247.2–0004	0.30 ^{0.60} _{0.60}	–12.57 ^{+0.33} _{–0.30}	13.32	8
J225003.5–594520	J2249.3–5943	1.71 ^{0.41} _{0.42}	–12.40 ^{+0.17} _{–0.14}	13.36	18
J225032.7+174918	J2250.3+1747	1.26 ^{0.42} _{0.43}	–12.64 ^{+0.18} _{–0.17}	14.05	13
J225045.7+330514	J2250.6+3308	1.63 ^{0.65} _{0.68}	–12.42 ^{+0.28} _{–0.19}	10.01	12
J230012.4+405223	J2300.0+4053	1.99 ^{0.09} _{0.09}	–11.20 ^{+0.03} _{–0.03}	135.26	181
J230351.7+555617	J2303.7+5555	1.84 ^{0.17} _{0.17}	–11.53 ^{+0.04} _{–0.04}	77.52	99
J230848.5+542612	J2309.0+5428	2.54 ^{0.27} _{0.26}	–12.19 ^{+0.07} _{–0.07}	47.02	46
J232127.1+511117	J2321.3+5113	2.55 ^{0.40} _{0.40}	–12.22 ^{+0.09} _{–0.09}	27.99	24
J232137.1–161926	J2321.6–1619	2.45 ^{0.12} _{0.12}	–11.61 ^{+0.03} _{–0.03}	101.96	119
J232653.3–412713	J2327.2–4130	1.97 ^{0.41} _{0.39}	–12.48 ^{+0.12} _{–0.12}	19.61	16
J232938.7+610111	J2329.8+6102	2.62 ^{0.18} _{0.18}	–11.28 ^{+0.06} _{–0.06}	94.22	120
J233626.4–842649	J2337.2–8425	2 ^{0.24} _{0.24}	–12.12 ^{+0.07} _{–0.07}	35.91	47
J235115.9–760017	J2351.9–7601	1.99 ^{0.21} _{0.20}	–12.03 ^{+0.06} _{–0.06}	56.64	51
J235824.10+382857	J2358.5+3827	2.15 ^{0.15} _{0.15}	–11.68 ^{+0.04} _{–0.04}	86	96
J235836.8–180717	J2358.6–1809	2.57 ^{0.10} _{0.10}	–11.55 ^{+0.03} _{–0.03}	125.82	135

Table 4. RF classification results for the unassociated sources and paired excesses. We used the grid-search optimized RF parameters to determine the blazar probabilities. Available at CDS via anonymous ftp to cdsarc.u-strasbg.fr (130.79.128.5) or via <http://cdsarc.u-strasbg.fr/viz-bin/qcat?J/AJ>

<i>Swift</i> X-ray excess	3FGL gamma-ray source	X-ray excess RA	X-ray excess Decl	Blazar Prob.	Categorization
SwF3	3FGL	(J2000)	(J2000)	P_{blzr}	
J000805.3+145018	J0008.3+1456	00 08 05.27	+14 50 18.5	0.976	blazar
J003159.9+093615	J0031.6+0938	00 31 59.89	+09 36 15.9	0.979	blazar
J004859.5+422348	J0049.0+4224	00 48 59.45	+42 23 48.8	0.990	blazar
J012152.5-391544	J0121.8-3917	01 21 52.53	-39 15 44.7	0.943	blazar
J013255.1+593213	J0133.3+5930	01 32 55.11	+59 32 13.3	0.999	blazar
J015624.4-242003	J0156.5-2423	01 56 24.44	-24 20 03.4	1.000	blazar
J015852.4+010126	J0158.6+0102	01 58 52.44	+01 01 26.9	0.988	blazar
J020020.9-410933	J0200.3-4108	02 00 20.90	-41 09 33.9	1.000	blazar
J021210.6+532139	J0212.1+5320	02 12 10.55	+53 21 39.6	0.081	pulsar
J023854.1+255405	J0239.0+2555	02 38 54.11	+25 54 05.6	0.991	blazar
J024454.9+475117	J0244.4+4745	02 44 54.93	+47 51 17.5	0.817	
J025111.4-183115	J0251.1-1829	02 51 11.39	-18 31 15.1	0.966	blazar
J025857.4+055243	J0258.9+0552	02 58 57.44	+05 52 43.7	0.996	blazar
J034050.0-242259	J0340.4-2423	03 40 50.02	-24 22 59.2	0.995	blazar
J034158.1+314851	J0342.3+3148c	03 41 58.10	+31 48 51.7	0.841	
J034819.8+603506	J0348.4+6039	03 48 19.77	+60 35 06.6	0.986	blazar
J035051.2-281632	J0351.0-2816	03 50 51.24	-28 16 32.6	0.998	blazar
J035939.3+764627	J0359.7+7649	03 59 39.29	+76 46 27.5	0.999	blazar
J041433.2-084213	J0414.9-0840	04 14 33.20	-08 42 13.2	0.997	blazar
J042011.0-601504	J0420.4-6013	04 20 11.02	-60 15 04.8	0.998	blazar
J042749.8-670434	J0427.9-6704	04 27 49.76	-67 04 34.8	0.772	
J042958.7-305931	J0430.1-3103	04 29 58.74	-30 59 31.7	0.989	blazar
J043836.9-732919	J0437.7-7330	04 38 36.85	-73 29 19.9	0.994	blazar
J044722.5-253937	J0447.1-2540	04 47 22.52	-25 39 37.4	0.998	blazar
J045149.6+572140	J0451.7+5722	04 51 49.56	+57 21 40.6	0.993	blazar
J050650.1+032359	J0506.9+0321	05 06 50.08	+03 23 59.6	0.999	blazar

Table 4 *continued*

Table 4 (continued)

<i>Swift</i> X-ray excess SwF3	3FGL gamma-ray source 3FGL	X-ray excess RA (J2000)	X-ray excess Decl (J2000)	Blazar Prob. P_{blzr}	Categorization
J051641.4+101243	J0516.6+1012	05 16 41.44	+10 12 43.4	0.984	blazar
J052939.5+382321	J0529.2+3822	05 29 39.54	+38 23 21.4	0.777	
J053357.3-375754	J0533.8-3754	05 33 57.33	-37 57 54.6	0.920	blazar
J053559.3-061624	J0535.7-0617c	05 35 59.28	-06 16 24.1	0.999	blazar
J055940.6+304232	J0559.8+3042	05 59 40.58	+30 42 32.7	0.985	blazar
J070421.7-482645	J0704.3-4828	07 04 21.74	-48 26 45.3	0.990	blazar
J071046.2-102942	J0711.1-1037	07 10 46.18	-10 29 42.2	0.437	
J072547.5-054830	J0725.7-0550	07 25 47.51	-05 48 30.3	0.997	blazar
J074626.10-022551	J0746.4-0225	07 46 26.98	-02 25 51.8	0.965	blazar
J074724.8-492633	J0747.5-4927	07 47 24.78	-49 26 33.9	0.999	blazar
J080215.8-094214	J0802.3-0941	08 02 15.78	-09 42 14.0	0.998	blazar
J081338.1-035717	J0813.5-0356	08 13 38.10	-03 57 17.1	0.968	blazar
J082623.6-505742	J0826.3-5056	08 26 23.55	-50 57 42.5	0.806	
J082628.2-640415	J0826.3-6400	08 26 28.16	-64 04 15.5	0.941	blazar
J083843.4-282701	J0838.8-2829	08 38 43.37	-28 27 01.6	0.719	
J084831.8-694108	J0847.2-6936	08 48 31.82	-69 41 08.9	0.994	blazar
J085505.8-481517	J0855.4-4818	08 55 05.78	-48 15 17.9	0.130	
J091926.1-220043	J0919.5-2200	09 19 26.09	-22 00 43.6	0.995	blazar
J092818.4-525659	J0928.3-5255	09 28 18.40	-52 56 59.7	0.980	blazar
J093444.6+090355	J0935.2+0903	09 34 44.60	+09 03 55.8	0.807	
J093754.6-143349	J0937.9-1435	09 37 54.55	-14 33 49.1	0.999	blazar
J095249.5+071329	J0952.8+0711	09 52 49.52	+07 13 29.6	0.996	blazar
J101545.9-602938	J1016.5-6034	10 15 45.85	-60 29 38.1	0.213	
J102432.6-454428	J1024.4-4545	10 24 32.56	-45 44 28.5	1.000	blazar
J103332.4-503526	J1033.4-5035	10 33 32.38	-50 35 26.7	1.000	blazar
J103755.1-242546	J1038.0-2425	10 37 55.09	-24 25 46.0	0.981	blazar
J103831.1-581346	J1039.1-5809	10 38 31.12	-58 13 46.6	0.497	
J104939.4+154839	J1049.7+1548	10 49 39.44	+15 48 39.0	0.973	blazar
J105224.5+081409	J1052.0+0816	10 52 24.46	+08 14 09.5	0.994	blazar
J110025.5-205333	J1100.2-2044	11 00 25.46	-20 53 33.1	0.906	blazar

Table 4 continued

Table 4 (continued)

<i>Swift</i> X-ray excess SwF3	3FGL gamma-ray source 3FGL	X-ray excess RA (J2000)	X-ray excess Decl (J2000)	Blazar Prob.	Categorization
J110224.1-773339	J1104.3-7736c	11 02 24.13	-77 33 39.9	0.916	blazar
J111601.8-484222	J1116.7-4854	11 16 01.82	-48 42 22.6	0.966	blazar
J111715.2-533815	J1117.2-5338	11 17 15.15	-53 38 15.3	0.997	blazar
J111956.10-264322	J1119.8-2647	11 19 56.96	-26 43 22.2	0.995	blazar
J111958.9-220456	J1119.9-2204	11 19 58.93	-22 04 56.6	0.032	pulsar
J112042.4+071313	J1120.6+0713	11 20 42.35	+07 13 13.1	0.337	
J112504.2-580539	J1125.1-5803	11 25 04.21	-58 05 39.6	1.000	blazar
J112624.8-500806	J1126.8-5001	11 26 24.82	-50 08 06.8	0.991	blazar
J113032.7-780107	J1130.7-7800	11 30 32.65	-78 01 07.5	0.902	blazar
J113209.3-473853	J1132.0-4736	11 32 09.31	-47 38 53.8	0.981	blazar
J114600.8-063851	J1146.1-0640	11 46 00.77	-06 38 51.0	0.998	blazar
J114911.10+280719	J1149.1+2815	11 49 11.98	+28 07 19.9	0.985	blazar
J115514.5-111125	J1155.3-1112	11 55 14.54	-11 11 25.3	0.896	
J120055.1-143039	J1200.9-1432	12 00 55.07	-14 30 39.0	0.992	blazar
J121553.0-060940	J1216.6-0557	12 15 53.04	-06 09 40.6	0.988	blazar
J122014.4-245948	J1220.0-2502	12 20 14.43	-24 59 48.0	0.994	blazar
J122019.8-371414	J1220.1-3715	12 20 19.82	-37 14 14.1	0.999	blazar
J122127.4-062845	J1221.5-0632	12 21 27.38	-06 28 45.9	0.989	blazar
J122257.0+121438	J1223.2+1215	12 22 57.04	+12 14 38.5	0.986	blazar
J122536.7-344723	J1225.4-3448	12 25 36.66	-34 47 23.8	0.999	blazar
J123140.3+482148	J1231.6+4825	12 31 40.28	+48 21 48.9	0.993	blazar
J123204.2+165527	J1232.3+1701	12 32 04.22	+16 55 27.7	0.776	
J123235.9-372055	J1232.5-3720	12 32 35.87	-37 20 55.8	0.992	blazar
J123447.7-043253	J1234.7-0437	12 34 47.69	-04 32 53.9	0.976	blazar
J123726.6-705140	J1236.6-7050	12 37 26.61	-70 51 40.1	0.996	blazar
J124021.3-714858	J1240.3-7149	12 40 21.34	-71 48 58.3	0.973	blazar
J124919.5-280833	J1249.1-2808	12 49 19.46	-28 08 33.5	0.999	blazar
J124919.7-054540	J1249.5-0546	12 49 19.69	-05 45 40.2	1.000	blazar
J125058.4-494444	J1251.0-4943	12 50 58.43	-49 44 44.3	0.998	blazar
J125821.5+212351	J1258.4+2123	12 58 21.49	+21 23 51.7	0.865	

Table 4 continued

Table 4 (continued)

<i>Swift</i> X-ray excess SwF3	3FGL gamma-ray source 3FGL	X-ray excess RA (J2000)	X-ray excess Decl (J2000)	Blazar Prob.	Categorization
J130059.5-814809	J1259.3-8151	13 00 59.45	-81 48 09.6	0.992	blazar
J130128.9+333711	J1301.5+3333	13 01 28.85	+33 37 11.0	0.793	
J130832.0+034406	J1309.0+0347	13 08 32.00	+03 44 06.9	0.779	
J131140.3-623313	J1311.8-6230	13 11 40.25	-62 33 13.9	0.577	
J131552.8-073304	J1315.7-0732	13 15 52.84	-07 33 04.0	0.998	blazar
J132928.6-053135	J1329.1-0536	13 29 28.56	-05 31 35.4	0.995	blazar
J140514.7-611822	J1405.4-6119	14 05 14.67	-61 18 22.7	0.113	
J141045.2+740504	J1410.9+7406	14 10 45.24	+74 05 04.8	0.849	
J141133.3-072256	J1411.4-0724	14 11 33.30	-07 22 56.3	0.996	blazar
J142035.9-243021	J1421.0-2431	14 20 35.85	-24 30 21.9	0.901	blazar
J144544.5-593200	J1445.7-5925	14 45 44.49	-59 32 00.2	0.996	blazar
J151150.10+662450	J1512.3+6622	15 11 50.95	+66 24 50.1	0.988	blazar
J151256.6-564027	J1512.8-5639	15 12 56.57	-56 40 27.3	0.865	
J151319.0-372015	J1513.3-3719	15 13 19.03	-37 20 15.0	0.977	blazar
J151649.8+263635	J1517.0+2637	15 16 49.82	+26 36 35.2	0.995	blazar
J152603.0-083146	J1525.8-0834	15 26 03.03	-08 31 46.2	0.785	
J152818.2-290256	J1528.1-2904	15 28 18.18	-29 02 56.8	0.981	blazar
J154150.1+141441	J1541.6+1414	15 41 50.12	+14 14 41.2	0.983	blazar
J154343.6-255607	J1544.1-2555	15 43 43.60	-25 56 07.6	0.804	
J154459.2-664147	J1545.0-6641	15 44 59.17	-66 41 47.8	0.991	blazar
J154946.4-304502	J1549.9-3044	15 49 46.41	-30 45 02.3	0.883	
J161543.2-444921	J1615.6-4450	16 15 43.18	-44 49 21.1	0.966	blazar
J162437.8-423144	J1624.8-4233	16 24 37.81	-42 31 44.3	0.986	blazar
J162607.8-242736	J1626.2-2428c	16 26 07.79	-24 27 36.2	0.330	
J162743.0+322102	J1627.8+3217	16 27 43.00	+32 21 02.4	0.776	
J165338.2-015837	J1653.6-0158	16 53 38.15	-01 58 37.0	0.045	pulsar
J170409.6+123423	J1704.1+1234	17 04 09.60	+12 34 23.0	0.977	blazar
J170433.9-052840	J1704.4-0528	17 04 33.91	-05 28 40.7	0.986	blazar
J170521.6-413436	J1705.5-4128c	17 05 21.56	-41 34 36.9	0.749	
J172142.1-392204	J1721.8-3919	17 21 42.13	-39 22 04.7	0.929	blazar

Table 4 continued

Table 4 (continued)

<i>Swift</i> X-ray excess SwF3	3FGL gamma-ray source 3FGL	X-ray excess RA (J2000)	X-ray excess Decl (J2000)	Blazar Prob.	Categorization
J172858.2+604359	J1729.0+6049	17 28 58.17	+60 43 59.9	0.995	blazar
J173250.5+591233	J1732.7+5914	17 32 50.51	+59 12 33.8	0.999	blazar
J173508.1-292955	J1734.7-2930	17 35 08.07	-29 29 55.4	0.496	
J174511.10-225455	J1744.7-2252	17 45 11.98	-22 54 55.7	0.177	
J175316.4-444822	J1753.6-4447	17 53 16.43	-44 48 22.0	0.668	
J175359.7-292909	J1754.0-2930	17 53 59.69	-29 29 09.0	0.165	
J180351.7+252607	J1804.1+2532	18 03 51.72	+25 26 07.0	0.780	
J180425.0-085002	J1804.5-0850	18 04 25.02	-08 50 02.5	0.966	blazar
J181307.6-684713	J1813.6-6845	18 13 07.62	-68 47 13.2	0.909	blazar
J181720.4-303257	J1817.3-3033	18 17 20.35	-30 32 57.8	0.985	blazar
J182914.0+272901	J1829.2+2731	18 29 14.00	+27 29 01.8	0.713	
J182915.5+323432	J1829.2+3229	18 29 15.50	+32 34 32.4	0.851	
J183659.5-240027	J1837.3-2403	18 36 59.46	-24 00 27.9	0.455	
J184433.1-034627	J1844.3-0344	18 44 33.14	-03 46 27.4	0.020	pulsar
J184833.10+323249	J1848.6+3232	18 48 33.96	+32 32 49.6	0.503	
J185520.0+075138	J1855.6+0753	18 55 20.02	+07 51 38.6	0.747	
J185606.6-122147	J1856.1-1217	18 56 06.60	-12 21 47.7	0.894	
J190444.5-070743	J1904.7-0708	19 04 44.53	-07 07 43.1	0.968	blazar
J192242.1-745354	J1923.2-7452	19 22 42.10	-74 53 54.9	0.980	blazar
J193420.1+600138	J1934.2+6002	19 34 20.08	+60 01 38.2	0.999	blazar
J194633.6-540235	J1946.4-5403	19 46 33.57	-54 02 35.1	0.042	pulsar
J195149.7+690719	J1951.3+6909	19 51 49.66	+69 07 19.2	0.971	blazar
J195800.3+243803	J1958.1+2436	19 58 00.28	+24 38 03.8	0.997	blazar
J200635.7+015222	J2006.6+0150	20 06 35.73	+01 52 22.4	0.861	
J201020.3-212434	J2010.0-2120	20 10 20.25	-21 24 34.2	0.737	
J201525.3-143204	J2015.3-1431	20 15 25.25	-14 32 04.7	0.999	blazar
J203027.9-143919	J2030.5-1439	20 30 27.92	-14 39 19.0	0.997	blazar
J203450.9-420038	J2034.6-4202	20 34 50.88	-42 00 38.1	0.988	blazar
J203935.8+123001	J2039.7+1237	20 39 35.76	+12 30 01.8	0.719	
J204351.5+103407	J2044.0+1035	20 43 51.54	+10 34 07.7	0.921	blazar

Table 4 continued

Table 4 (continued)

<i>Swift</i> X-ray excess SwF3	3FGL gamma-ray source 3FGL	X-ray excess RA (J2000)	X-ray excess Decl (J2000)	Blazar Prob.	Categorization
J204806.3-312011	J2047.9-3119	20 48 06.25	-31 20 11.5	0.901	blazar
J205350.8+292312	J2053.9+2922	20 53 50.77	+29 23 12.4	0.914	blazar
J205357.9+690517	J2054.3+6907	20 53 57.94	+69 05 17.7	0.787	
J205950.4+202905	J2059.9+2029	20 59 50.44	+20 29 05.0	0.984	blazar
J210940.0+043958	J2110.0+0442	21 09 40.04	+04 39 58.3	1.000	blazar
J211522.2+121801	J2115.2+1215	21 15 22.17	+12 18 01.7	1.000	blazar
J212051.6-125300	J2120.4-1256	21 20 51.55	-12 53 00.4	0.851	
J212601.5+583148	J2125.8+5832	21 26 01.49	+58 31 48.3	0.630	
J212729.3-600102	J2127.5-6001	21 27 29.30	-60 01 02.1	0.970	blazar
J214247.5+195811	J2142.7+1957	21 42 47.47	+19 58 11.9	1.000	blazar
J214429.5-563849	J2144.6-5640	21 44 29.48	-56 38 49.7	0.918	blazar
J215046.5-174956	J2150.5-1754	21 50 46.46	-17 49 56.0	0.913	blazar
J215122.10+415634	J2151.6+4154	21 51 22.99	+41 56 34.5	0.999	blazar
J220941.4-045108	J2209.8-0450	22 09 41.35	-04 51 08.2	0.933	blazar
J222911.2+225456	J2229.1+2255	22 29 11.17	+22 54 56.1	0.998	blazar
J224437.0+250344	J2244.6+2503	22 44 37.00	+25 03 44.3	0.930	blazar
J224710.1-000512	J2247.2-0004	22 47 10.11	-00 05 12.1	0.488	
J225003.5-594520	J2249.3-5943	22 50 03.45	-59 45 20.4	0.993	blazar
J225032.7+174918	J2250.3+1747	22 50 32.71	+17 49 18.4	0.980	blazar
J225045.7+330514	J2250.6+3308	22 50 45.65	+33 05 14.8	0.647	
J230012.4+405223	J2300.0+4053	23 00 12.36	+40 52 23.3	0.992	blazar
J230351.7+555617	J2303.7+5555	23 03 51.70	+55 56 17.9	0.968	blazar
J230848.5+542612	J2309.0+5428	23 08 48.49	+54 26 12.0	1.000	blazar
J232127.1+511117	J2321.3+5113	23 21 27.12	+51 11 17.8	1.000	blazar
J232137.1-161926	J2321.6-1619	23 21 37.05	-16 19 26.2	0.999	blazar
J232653.3-412713	J2327.2-4130	23 26 53.32	-41 27 13.4	0.993	blazar
J232938.7+610111	J2329.8+6102	23 29 38.70	+61 01 11.6	1.000	blazar
J233626.4-842649	J2337.2-8425	23 36 26.35	-84 26 49.5	0.989	blazar
J235115.9-760017	J2351.9-7601	23 51 15.89	-76 00 17.6	0.994	blazar
J235824.10+382857	J2358.5+3827	23 58 24.95	+38 28 57.2	1.000	blazar
J235836.8-180717	J2358.6-1809	23 58 36.75	-18 07 17.9	1.000	blazar